Significance of diapycnal mixing within the Atlantic Meridional Overturning Circulation

Laura Cimoli[1,8], Ali Mashayek[2], Helen L. Johnson[3], David P. Marshall[1], Alberto C. Naveira Garabato[4], Caitlin B. Whalen[5], Clément Vic[6], Casimir de Lavergne[7], Matthew H. Alford[8], Jennifer A. MacKinnon[8], Lynne D. Talley[8]

[1]Department of Physics, University of Oxford
[2]Environmental Engineering & Grantham Institute of Climate and Environment, Imperial College, London
[3]Department of Earth Sciences, University of Oxford
[4]School of Ocean and Earth Science, University of Southampton
[5]Applied Physics Laboratory, University of Washington, Seattle
[6]Laboratoire d'Océanographie Physique et Spatiale, University of Brest, CNRS, IRD, Ifremer, Plouzané, France
[7]LOCEAN Laboratory, Sorbonne Université-CNRS-IRD-MNHN, Paris, France
[8]Scripps Institution of Oceanography, University of California San Diego

Key Points:

- The cross-density mixing of water and tracers is quantified from observation-based estimates and numerical simulations in the Atlantic Ocean.
- Up to 4 Sv of NADW upwells diapycnally in the ocean interior, with potentially larger, spatially variable, diapycnal up- and downwelling.
- Tracer mixing in the deep Atlantic Ocean can significantly modify pathways and ventilation rates of tracers upwelling in the Southern Oceans

Corresponding author: Laura Cimoli, lcimoli@ucsd.edu

Abstract

Diapycnal mixing shapes the distribution of climatically-important tracers, such as heat and carbon, as these are carried by dense water masses in the ocean interior. Here, we analyze a suite of observation-based estimates of diapycnal mixing to assess its role within the Atlantic Meridional Overturning Circulation. The rate of water mass transformation in the Atlantic Ocean's interior shows that there is a robust buoyancy increase in the North Atlantic Deep Water (NADW), with a diapycnal circulation of up to 4 Sv between 24°N and 32°S in the Atlantic Ocean. Moreover, tracers within the southward-flowing NADW may undergo a substantial diapycnal transfer, equivalent to hundreds of metres in the vertical. This result is confirmed with a zonally-averaged numerical model of the AMOC and indicates that tracer mixing can lead to divergent global pathways and ventilation timescales following the upwelling of tracers in the Southern Ocean. These results point to the need for a realistic mixing representation in climate models in order to understand and credibly project the ongoing climate change.

Plain Language Summary

The Atlantic Ocean meridional overturning circulation plays a key role in regulating the global heat and carbon budgets by inter-hemispheric transport of anthropogenic and natural tracers as well as water masses. While most of this transport occurs along nearly horizontal density surfaces in the ocean interior, vertical transport across density levels is key to bringing deep waters back to the surface. Such cross-density transport is facilitated mainly by the internal waves breaking into turbulence and near boundary processes. This work employs a host of observation-based estimates of turbulence in the Atlantic Ocean to (i) better quantify the contribution of cross-density mixing to the inter-hemispheric Atlantic circulation, and (ii) discuss the potential implications for pathways and residence times of tracers carried from the North Atlantic to the Southern Ocean. This work calls for a more careful representation of turbulence-induced vertical mixing within the Atlantic Ocean in climate models to better understand and project the ongoing climate change.

1 Introduction

The Atlantic Meridional Overturning Circulation (AMOC) constitutes a key component of the global ocean circulation, and plays a central role in the regulation, variability and anthropogenic change of our climate. The AMOC is the primary contributor to the redistribution of heat in the Atlantic Ocean, transporting heat northward in both hemispheres (Forget & Ferreira, 2019). Further, it exerts a profound influence on the sequestration of tracers, such as oxygen and anthropogenic carbon, that are taken up in the process of dense water formation (Gruber et al., 2019).

The AMOC is an overturning cell, encompassing net southward transport of dense waters and net northward return of lighter waters (Figure 1a). The dense southward-flowing waters are produced through surface transformation of lighter waters in the subpolar North Atlantic, and are additionally sourced by entrainment of Mediterranean Water, and by diapycnal exchanges with northward-flowing intermediate and abyssal waters (Reid, 1994; Talley, 1996). Together, these diverse sources give rise to North Atlantic Deep Water (NADW), which flows southward at a depth of ∼1000-4000 m and surfaces in the Southern Ocean (Figure 1). Inverse models and ocean state estimates (e.g. Ganachaud, 2003; Talley et al., 2003; Lumpkin & Speer, 2007; Talley, 2013; Forget et al., 2015), as well as direct measurements (e.g. the RAPID-MOCHA array – Cunningham et al., 2007; McCarthy et al., 2015; Srokosz & Bryden, 2015), suggest that the maximum southward transport of the AMOC is around 16-24 Sv (where 1 Sv = 10^6 m^3s^{-1}), as shown in Figure 1a from the Estimating the Circulation and Climate of the Ocean (ECCO) state estimate. Underlying the AMOC cell is a weaker overturning cell, in which abyssal Antarctic Bottom Water (AABW) flows northward after sinking to the seafloor around Antarctica (Figure 1a).

NADW is often conceptualized as an adiabatic flow, i.e. directed along density surfaces (isopycnals; see Figure 1a), between the North Atlantic and the Southern Ocean, where density surfaces outcrop (Marshall & Speer, 2012; Cessi, 2019). Several studies, in particular stemming from theoretical investigations or idealized numerical simulations, have suggested that NADW returns to the surface mainly via wind-driven upwelling along the steeply sloping isopycnals outcropping in the Southern Ocean, without any significant role for diapycnal mixing (e.g. Toggweiler & Samuels, 1998; Gnanadesikan, 1999; Wolfe & Cessi, 2011; Marshall & Speer, 2012; Johnson et al., 2019).

However, observation-based inverse models (e.g. Talley et al., 2003; Lumpkin & Speer, 2007) and the ECCO state estimate (Forget et al., 2015; Cessi, 2019) show a reduction in AMOC's transport by about 2-10 Sv between 24°N and 32°S, largely driven by downward diffusion of low-latitude surface heat gain (Talley, 2013). An important further contribution to such reduction may be effected by diapycnal mixing near the Atlantic's topographic boundaries, along which a substantial fraction of the AMOC transport occurs (de Lavergne et al., 2022). Several recent investigations of the connection between diapycnal mixing and the turbulent transformation of water masses, especially in regions of topographically-enhanced turbulence, have hypothesized that diapycnal mixing induces diapycnal downwelling (i.e. a densification of water masses) in the ocean interior, and diapycnal upwelling (i.e. a lightening of water masses) in the proximity of topographic boundaries (de Lavergne, Madec, Sommer, et al., 2016; Ferrari et al., 2016; Mashayek, Salehipour, et al., 2017; McDougall & Ferrari, 2017). Globally integrated, these transformations have been proposed to result in a net dense-to-light water mass conversion of abyssal waters. The implications of this emerging paradigm for the AMOC's rate and structure are not yet clear.

Importantly, the diapycnal transfer of water masses (i.e. of mass) does not generally explain how tracers (such as anthropogenic carbon, oxygen or nutrients) are redistributed across different water masses by diapycnal mixing. This is because the tracer evolution will also depend on a diffusive diapycnal tracer transport, occurring without a diapycnal mass transfer (Groeskamp et al., 2019). If tracers mix within NADW or with surrounding layers, they may outcrop in substantially different regions and dynamical regimes of the Southern Ocean, and join distinct downstream branches of the overturning circulation. For example, the transport analysis by Lumpkin and Speer (2007) indicates that the neutral density (Jackett & McDougall, 1997) surface $\gamma^n = 27.6$ roughly separates lighter and denser NADW components with different fates. The former NADW class transforms into lighter waters and returns to the North Atlantic on decadal-to-centennial timescales, whereas the latter class ($\gamma^n > 27.6$) transforms into AABW near Antarctica and re-emerges only on millennial time scales (Sloyan & Rintoul, 2001; Santoso et al., 2006; Lumpkin & Speer, 2007; Naveira-Garabato et al., 2014).

To illustrate the importance of the AMOC in regulating tracer distributions, Figure 1b shows the depth-integrated concentration of anthropogenic carbon from an observational climatology (GLobal Ocean Data Analysis Project, GLODAP; Lauvset et al. (2016)). The formation and southward flow of NADW is reflected in the deeper and faster penetration of anthropogenic carbon in the Atlantic Ocean, where the areal storage is nearly double that in the Pacific Ocean, where there is no deep-water formation (Gruber et al., 2019).

In this study, we investigate the significance of diapycnal mixing for the AMOC and for the transfer of tracers between the AMOC's different water masses, with a focus on the southward-flowing NADW. We employ observation-based, basin-wide estimates of diapycnal mixing, comprising of: (i) direct measurements of the rate of dissipation of turbulent kinetic energy (hereafter dissipation rate) by microstructure probes (Waterhouse et al., 2014); (ii) internal wave dissipation rate estimates from strain-based parameterizations (M. Gregg & Kunze, 1991; Wijesekera et al., 1993; M. C. Gregg et al., 2003; Kunze et al., 2006; Polzin et al., 2014) applied to either Argo float measurements (Whalen et al., 2012, 2015) or hydrographic sections (Kunze, 2017b); (iii) an energy-constrained, observationally-tested parameterization of internal tide-induced dissipation rate (de Lavergne et al., 2020); and

(iv) a bulk estimate of the diapycnal diffusivity (the rate of diapycnal mixing) from an inverse model (Lumpkin & Speer, 2007). These estimates have significant uncertainties, some intrinsic to the parameterizations used to infer mixing rates (ii, iii), and others due to sampling limitations (i,ii,iv). However, the combination of different approaches enables a comprehensive look at the Atlantic-wide patterns of diapycnal mixing and their implications for ocean circulation and tracer distributions.

2 Diapycnal mixing estimates in the Atlantic Ocean

Diapycnal mixing in the ocean interior is mainly generated by breaking internal waves, and is typically quantified by relating the rate at which turbulent kinetic energy is dissipated during wave breaking events, ϵ, to a turbulent diffusivity coefficient, κ. Diapycnal mixing contributes to the irreversible transformation of a water parcel's density. Defining buoyancy as $b = -(g/\rho_0)(\rho - \rho_0)$, where ρ_0 is a reference density, and $N^2 = \partial_z b$ as the buoyancy frequency squared, the buoyancy flux can be approximated, following Osborn (1980), as

$$\mathcal{M} \approx -\kappa N^2 \approx \Gamma\epsilon, \tag{1}$$

which indicates that the buoyancy flux, $\mathcal{M}$, is a fraction of the rate at which energy is lost to viscous dissipation, ϵ. This fraction is expressed by the turbulent flux coefficient Γ, which here we take to be a constant value of 0.2, as it is pertinent to shear-driven turbulence and commonly assumed in physical oceanography (e.g. M. Gregg et al. (2018); Caulfield (2020)). While Γ can be spatially variable (Mashayek & Peltier, 2013; Bouffard & Boegman, 2013; Mashayek, Salehipour, et al., 2017; de Lavergne, Madec, Le Sommer, et al., 2016; Cimoli et al., 2019; Spingys et al., 2021), the implications of such variability for mixing are still not well understood on basin scales.

The turbulence estimates collated here are in the form of either ϵ or κ, from which we infer the buoyancy flux across different neutral density surfaces (Equation 1). The four estimates we use, described in detail in the Supplementary Materials, are:

1. Estimates of ϵ from a strain-based parameterization applied to Argo float hydrographic data (an updated version of the dataset used in Whalen et al. (2012, 2015) with higher spatio-temporal resolution). Figures 2a,b show the localized estimates of dissipation rate on two different density surfaces, both lying at depths shallower than 2000 m, where Argo data stops. Available estimates have been interpolated to avoid gaps in areas where Argo data are not available in sufficient density. The Argo-based dissipation estimates display marked spatial variability, with intense dissipation in regions of rough topography, elevated tidal and wind energy inputs, or high eddy kinetic energy (Whalen et al., 2012).
2. Estimates of ϵ from a strain-based parameterization applied to CTD (Conductivity, Temperature and Depth) hydrographic profiles from Kunze (2017a, 2017b). These estimates have been combined with the dissipation rate directly measured by microstructure profilers in Waterhouse et al. (2014), which mainly improve the quality of the estimates below 2000 m (not shown), and have been gridded on a 1° horizontal grid (Figures 2c-e). These estimates agree with the Argo-based data (Figures 2a,b), both qualitatively, identifying the regions of enhanced turbulence (e.g. in the northwest Atlantic Ocean, an area of enhanced eddy activity, and where the Mid-Atlantic Ridge reaches shallow depths) and weak turbulence (e.g. in the Angola basin); and quantitatively, returning the same magnitude of ϵ (with a few exceptions in the mid-Atlantic). The use of hydrographic and microstructure data has the advantage of providing a continuous estimate throughout the full water column based on observations. For example, Figure 2e shows ϵ on the neutral density surface $\gamma^n = 28.1$, where Argo-based estimates are not available. Finescale parameterizations can underestimate high dissipation values over rough topography (de Lavergne et al., 2020), and return an overall decrease of ϵ with depth, suggesting that most of the turbulent

kinetic energy is dissipated in pycnocline waters (Kunze (2017b); Figures 2a-b and 2c-e).

3. Estimates of tide-generated ϵ from de Lavergne et al. (2020), which take into account both the contributions of locally-breaking (high-mode) and long-distance propagating (low-mode) internal tides. This dataset is constructed by accounting for four different dissipative processes (wave-wave interactions, scattering by abyssal hills, dissipation over critical slopes, and shoaling), as well as the waves' horizontal and vertical propagation. de Lavergne et al. (2020) compared this estimate with the dissipation measured by microstructure profilers and parameterized from Argo float data, showing an overall good agreement as discernible in Figure 2. We will refer to this estimate as "tidally-driven" mixing, although in the calculation of the buoyancy flux we also take into account the contribution of geothermal heating from Davies and Davies (2010).
4. The estimates of turbulence outlined above suffer from two substantial limitations: they lack full spatial coverage (across the globe, in depth and especially close to ocean boundaries), and/or depend on a range of underlying assumptions. As such, it is important to assess inferences from these estimates against bulk diagnostics of basin-scale diapycnal mixing. Here, we consider the inversely-estimated diffusivity from Lumpkin and Speer (2007), which stems from combining WOCE (World Ocean Circulation Experiment) hydrographic sections and observation-based datasets of air-sea exchanges of heat and freshwater to quantify the global meridional overturning circulation. Lumpkin and Speer (2007) divided the ocean into boxes bounded by hydrographic sections, and estimated a profile of the turbulent diffusivity in each box as a bulk average across each density surface. This bulk estimate does not provide any information on the spatial pattern of mixing within the large region contained by a box, nor on the processes that underpin the mixing. However, it indicates the order-of-magnitude rate of mixing required to sustain the reconstructed meridional overturning. Processes that cannot be estimated from other observations, and may thus be missing from the first three estimates, are implicitly included in the bulk estimate.

Note that estimate (3) excludes the dissipation associated with lee waves excited through interaction of geostrophic motions with rough topography. In ocean basins north of the Southern Ocean, the lee wave contribution is modest compared to that of internal tides (Nikurashin & Ferrari, 2011; Waterman et al., 2014). Also unaccounted for is the contribution of the wind-induced near-inertial shear in the upper ocean, as $\sim$70% of the wind energy is is dissipated in the top 200 m (Zhai et al., 2009). The total near-inertial wind power that makes it to the deep ocean is a small fraction of the tidal power (M. H. Alford, 2020).

3 Results

3.1 Diapycnal circulation and water mass transformation rates within the AMOC

Internal wave-driven turbulence can lead to the irreversible transformation of water masses, which may become either lighter or denser. The sign and the rate of the water mass transformation depend on the diapycnal divergence of the buoyancy flux: water masses are transformed only if mixing is vertically non-homogeneous, i.e. if there is a diffusive convergence or divergence of buoyancy. Water (mass) moves across density surfaces at the diapycnal velocity (Ferrari et al., 2016):

$$w^* = \frac{\partial_z \mathcal{M}}{\partial_z b}. \tag{2}$$

The diapycnal velocity is positive, and waters become lighter, when the buoyancy flux arising due to mixing ($\mathcal{M}$) decreases with depth, for example when there is surface-intensified mixing, or in the bottom boundary layer where $\mathcal{M} \to 0$ towards the ocean floor (de Lavergne,

Madec, Sommer, et al., 2016; Ferrari et al., 2016). In calculating the buoyancy flux divergence at the bottom, a geothermal heat flux is included following Adcroft et al. (2001); Mashayek et al. (2013). Conversely, diapycnal velocity is negative, and waters become denser, when mixing intensifies with depth, for example in the ocean interior near rough topography (de Lavergne, Madec, Sommer, et al., 2016; Ferrari et al., 2016; McDougall & Ferrari, 2017). Note that Equation (2) ignores effects related the non-linearity of the equation of state: these effects are quasi negligible at the depths (> 1000 m) and latitudes considered here (Klocker & McDougall, 2010; de Lavergne, Madec, Sommer, et al., 2016).

As an example, diapycnal velocities inferred from the estimates of tidally-driven diapycnal mixing are shown on the density surfaces $\gamma^n = 27.6$ and $\gamma^n = 28.1$ (Figures 3a,b). Diapycnal upwelling (red) occurs in the upper ocean, where most of the energy is dissipated (Kunze, 2017b; de Lavergne et al., 2020), and along sloping topography in the bottom boundary layer (de Lavergne, Madec, Sommer, et al., 2016; Ferrari et al., 2016; McDougall & Ferrari, 2017). Diapycnal downwelling (blue) takes place mainly in the deep ocean interior, where the buoyancy flux increases towards the bottom over rough topography, following microstructure measurements (e.g. St Laurent et al. (2001)).

The water mass transformation rate across a neutral density surface γ^n_* in the ocean interior is given by the integral of the diapycnal velocity over that density surface:

$$\mathcal{D}(\gamma^n_*) = -\iint_{A(\gamma^n_*)} w^* \cdot \widehat{\mathbf{n}}\, dA \tag{3}$$

where $\widehat{\mathbf{n}}$ is the unit vector normal to the density surface, A is the area of the density surface, and the minus sign is used such that water mass transformation is positive when water goes from denser to lighter (following (Ferrari et al., 2016)). The net transformation rate is the residual of transformation along topographic boundaries, which generates along-boundary upwelling, and transformation in the ocean interior, which generates diapycnal up/downwelling depending on the sign of $\partial\mathcal{M}/\partial z$. Of the three localized estimates of diapycnal mixing used here, only the estimate of tidally-driven mixing allows for a full investigation of the relative importance of the boundary and interior contributions; neither the Argo-based nor the CTD- and microstructure-based estimates have sufficient resolution to adequately capture the water mass transformation along the boundaries.

Figure 3c shows the water mass transformation rate $\mathcal{D}(\gamma^n)$ for the tidally-driven mixing estimates, spanning the density levels of the southward-flowing AMOC waters ($\gamma^n = 27.6 - 28.15$) and the abyssal waters below ($\gamma^n > 28.15$). The contributions of water mass transformation along topographic boundaries and in the ocean interior are represented by the empty red and blue bars, respectively, while the net water mass transformation rate integrated over the entire isopycnal area between 48°N and 32°S is denoted by the filled blue bars. The net water mass transformation is positive for most of the density surfaces analysed, indicating a lightening of these water masses. This result is consistent with the findings of de Lavergne, Madec, Sommer, et al. (2016), Ferrari et al. (2016) and Kunze (2017a), and agrees with the notion that diapycnal mixing in the deep ocean acts to raise dense waters back to shallower depths, contributing to the AMOC's closure.

Figure 3c also highlights that, for light density levels, waters upwell both in the interior and in the proximity of the boundary, whereas as waters start interacting with rough topography, the dissipation tends to increase toward the bottom, generating opposing patterns of up- and downwelling. These patterns are particularly evident at $\gamma^n = 28.1$, the density surface with the largest area in contact with topography (de Lavergne et al., 2017), and hence the largest water mass transformation in the abyssal ocean.

While the net water mass transformation across $\gamma^n = 28.1$ is about 3 Sv, the red and blue bars in Figure 3c indicate more than 21 Sv and 18 Sv of diapycnal upwelling and downwelling, respectively. Thus, although the residual suggests a modest turbulent exchange across these density surfaces, the magnitude and pattern of the two contributions indicate

that tracers may experience significant up- or downwelling, depending on their distribution, i.e. on the extent to which tracers are stirred laterally, homogenized or transported away from the boundaries, as well as on the spatial configuration of diapycnal upwelling and downwelling. Available tracer observations do not have the spatio-temporal resolution to explore this hypothesis, which has been examined in idealized numerical simulations (Mashayek et al., 2015; Ferrari et al., 2016; Mashayek, Ferrari, et al., 2017; Holmes et al., 2019; Drake et al., 2020).

3.2 Estimates of Atlantic-integrated mixing

The Atlantic-integrated (48°N to 32°S) residual water mass transformation rate, based on each of the estimates of diapycnal mixing discussed above, is shown in Figure 4a. The density range identified by the pink band ($\gamma^n = 27.2-27.7$) indicates the approximate boundary between the net southward and northward flows of the AMOC, which varies with latitude. Following Lumpkin and Speer (2007), southward-flowing AMOC waters are denser than $\gamma^n \simeq 27.7$ in the Northern Hemisphere, but the boundary between net southward/northward flows moves to lighter waters (up to $\gamma^n \simeq 27.2$) in the Southern Hemisphere. The boundary between the net deep southward-flowing and the net abyssal northward-flowing waters in the Atlantic Ocean is around $\gamma^n = 28.15$ (Burke et al., 2015).

The net transformation rate is positive for most density classes shown in Figure 4a, indicating a net diapycnal upwelling, i.e. a lightening of deep waters. For waters denser than $\gamma^n = 27.5$, the four different estimates show a consistent vertical structure: the transformation rate is largest within the southward NADW flow, particularly in the $\gamma^n = 27.7 - 27.9$ density range, it weakens around $\gamma^n = 28 - 28.05$, and increases again below $\gamma^n = 28.1$. That water mass transformations calculated from different mixing estimates, using data collected via distinct approaches and employing various parameterizations or assumptions, exhibit similar patterns, gives us confidence that we can draw general conclusions on the basin-integrated picture.

The water mass transformation rate estimated from Argo floats is the smallest overall, with values up to ~ 0.8 Sv at $\gamma^n = 27.7 - 27.95$, and weaker values on the other density surfaces. The estimate based on CTD data and microstructure profiles (in yellow) results in transformation rates up to ~ 1.2 Sv within the southward NADW pathway ($\gamma^n = 27.65 - 27.95$), and smaller values for both lighter and denser isopycnals. The water mass transformation rate calculated from tidally-driven mixing (in green) reaches a maximum of ~ 3 Sv at $\gamma^n = 28.1$: this density surface has the largest area of contact with the bottom (de Lavergne et al., 2017), resulting in significant diapycnal transformation of deep waters, in agreement with previous studies (de Lavergne, Madec, Sommer, et al., 2016; Ferrari et al., 2016; de Lavergne et al., 2017; Kunze, 2017b; Mashayek, Salehipour, et al., 2017; Cimoli et al., 2019). The rates of water mass transformation for the tidally-driven mixing at lighter density classes are smaller, but still substantial. The bulk estimate from Lumpkin and Speer (2007) (in blue) returns the largest transformations, up to ~ 4 Sv at $\gamma^n = 27.8 - 27.9$, i.e. within the core of the southward NADW flow, and at $\gamma^n > 28.1$, i.e. in the abyssal waters.

3.3 Implications for diapycnal transfers within the AMOC

Given the amount of mixing found within the NADW layer (Figure 4a), it is not unreasonable to expect that water and tracers carried by the southward-flowing limb of the AMOC may undergo substantial diapycnal transfers. To elucidate this possibility, we calculate a diffusive length scale, representing the characteristic vertical distance over which diapycnal mixing can move water and tracers as they are transported in the NADW flow from the North Atlantic (48°N) to the Southern Ocean (32°S). Diffusion across density surfaces depends on the ambient effective turbulent buoyancy flux ($\mathcal{M}$), density stratification (N^2) and transit time through the length of the Atlantic (Δt).

Following Fick's law of diffusion, the diffusive length scale is

$$\mathcal{L} = 2\sqrt{\frac{\langle \mathcal{M} \rangle}{\langle N^2 \rangle} \Delta t} \; = \; 2\sqrt{\kappa \Delta t}, \tag{4}$$

where $\langle \mathcal{M} \rangle$ is the buoyancy flux averaged over each isopycnal and is inferred from the four mixing estimates described above, and the average N^2 is calculated from WOCE hydrographic climatology. A transit time Δt for waters to travel from 48°N to 32°S is estimated based on observations of meridional transport in the North Atlantic from the RAPID-MOCHA array. As most water parcels do not travel directly from the source region to the Southern Ocean in the strong boundary current (see for example Fine et al. (2002); Bower et al. (2009); Holzer et al. (2010); Rhein et al. (2015); MacGilchrist et al. (2017)), we infer the transit time from a cross-basin-average meridional velocity. A decadal average of the transport at 26°N (Smeed et al., 2014) is used to calculate an average meridional velocity at different depths from the transport maximum at $\sim$ 1100 m to $\sim$ 4500 m, where the zonally integrated transport changes direction (i.e. below 4500 m the transport is northward). This average velocity is used to compute a depth-dependent transit time. The mean depth of each density surface, shown along the right-hand y-axis in Figure 4b, is then used to convert this into an estimate of the mean transit time for waters at any given density. The transit time is $\sim$ 100 years at $\gamma^n = 27.6$, whose average depth is close to the depth of the maximum overturning streamfunction (Smeed et al., 2014), and $\sim$ 350 years at $\gamma^n = 28.2$. This range of transit times agrees with estimates of the inter-hemispheric transit time inferred from Antarctic and Arctic ice core data (e.g. Buizert et al., 2015).

Figure 4b shows the diffusive length scale corresponding to each of the water mass transformation estimates presented in Figure 4a. For the density classes associated with the core of the southward NADW flow, $\mathcal{L}$ lies between approximately 400 m and 2000 m - except for the diffusive length scale estimated from the bulk estimate diffusivity, which returns much larger values. Contextualizing these length scales with the mean depths of the density surfaces reported in Figure 4b suggests that mass and tracers can undergo sufficient mixing to transfer between water masses with substantially different fates. For example, a diffusive length scale of $\sim$ 800 - 1000 m at $\gamma^n = 27.9$ indicates that mixing could move waters and tracers from the core of the NADW flow to lighter water masses ($\gamma^n < 27.6$) that return to the North Atlantic after upwelling in the Southern Ocean. A diffusive length scale of $\sim$ 500 m at $\gamma^n = 27.6 - 27.7$ indicates that waters and tracers may be transferred from the NADW layer into the overlying northward branch of the AMOC, to be carried back to the North Atlantic and into contact with the atmosphere on a much shorter timescale than might otherwise be expected in the limit of interior adiabatic flow.

The diffusive length scale calculation relies on two restrictive assumptions: (i) the mean buoyancy flux here is computed from either the rate of dissipation of turbulent kinetic energy or the diapycnal diffusivity, integrated over each density class, so it is meaningful only in a bulk sense; and (ii) the diffusive scale is calculated based on buoyancy, thereby neglecting the heterogeneity of tracers on isopycnals. For a given tracer, both the tracer's spatial distribution and the spatial patterns of mixing are key to accurate quantification of the diapycnal transfers experienced by the tracer. When carried over regions of weak mixing, a tracer will experience only a minor vertical displacement; but in regions of intense mixing, the vertical tracer displacement could be much larger than the values shown here.

3.4 Diapycnal tracer transfers in a numerical model

In this section, we use a zonally-averaged model of the Atlantic Ocean to show that diapycnal mixing within the AMOC exerts a profound influence on the basin-wide distribution of tracers. Mixing influences tracer distributions (i) on short time scales, by altering the amount of transport across tracer gradients, and (ii) on long time scales, by modifying the ocean circulation and stratification.

We use the zonally-averaged model of the Atlantic Ocean by Nikurashin and Vallis (2012) which produces a realistic two-cell AMOC consistent with Figure 1a. Diapycnal mixing is the only component of their original model modified here. Figure 5 shows the overturning streamfunction for two different mixing representations: (i) a constant value of $\kappa = 3 \times 10^{-5}$ m^2/s, based on the quasi-constant (in the vertical) diffusivity inferred by Kunze (2017b), and (ii) a κ based on the bulk basin-wide estimate of Lumpkin and Speer (2007), hereafter κ_{LS07}. The latter overturning streamfunction exhibits a stronger abyssal cell, due to enhanced near-bottom mixing. The rates of overturning in both simulations agree reasonably well with those based on ECCO (in Figure 1a).

Figure 6 illustrates the time evolution of the concentration of a passive tracer for various configurations of diapycnal mixing (one configuration per row). To distinguish the short-time scale response of tracer to changes in mixing from the long-term response due to changes in the AMOC (caused by the mixing-induced changes to the AMOC), in some configurations different diffusivities are used for buoyancy and the passive tracer. For all cases, the simulation is first run until the overturning circulation reaches steady state, and a passive tracer is injected at the surface in the Northern Hemisphere with values increasing linearly from 0 at the equator to 1 at the northernmost point. The simulations are continued until the tracer finds its way to the Southern Ocean.

In the first configuration, referred to hereafter as the 'control run', both the passive tracer and buoyancy are subject to a constant modest vertical diffusivity of 3×10^{-5} m^2/s. The tracer sinks with the deep waters formed at the northern boundary and is advected southward within the NADW. Along the way to the Southern Ocean, a significant portion of the tracer is diffused upward towards lighter northward-flowing waters (note the overturning streamfunction contours in black) and a lesser portion mixes diapycnally with the underlying northward-flowing waters of the lower cell (shown with dashed streamlines).

In a second configuration (second row), enhanced mixing κ_{LS07} is applied only to the tracer, while keeping the mixing acting on the buoyancy field constant at the same value as in the control run. Thus, the overturning circulation remains the same as in the control run, while the tracer mixing is enhanced. The colored contours show the difference between the tracer concentration in this case and that in the control run. The net effect of enhanced tracer mixing is an increase in the upward diapycnal transfer of tracer towards the northward-flowing branch of the upper cell, as well as a downward diapycnal transfer into the abyssal cell. As a result, a lower concentration of tracer reaches the Southern Ocean via the southward-flowing NADW.

In a third configuration (third row), we do the opposite perturbation experiment: the tracer is diffused with the constant $\kappa = 3 \times 10^{-5}$ m^2/s (as in the control run), while the buoyancy field is subject to κ_{LS07}. For this case, we first let the simulation run forward until a new steady circulation is obtained, and then release the tracer. The tracer anomalies naturally reflect the change in circulation: the enhanced mixing strengthens and inflates the abyssal cell (as can be seen by comparing the dashed streamlines with those from the top two rows). As a result, more tracer ends up in the lower cell at the expense of the tracer concentration in the upper cell.

Finally, in a fourth configuration (fourth row), both the buoyancy field and the passive tracer are subject to κ_{LS07}. The tracer anomalies in this case reflect the combined impacts of mixing-driven changes in the circulation (as in the third row) and changes due to the direct influence of mixing on the tracer (second row). The total effect on timescales of a few centuries is a larger concentration in the abyss and in the upper Atlantic, at the expense of mid-depth and Southern Ocean waters.

In summary, Figure 6 makes three important points. First, enhanced diapycnal mixing in the Atlantic Ocean significantly changes the vertical distribution of the tracer by acting on the tracer gradients. Second, enhanced mixing significantly redistributes the tracer in

the vertical by changing the underlying, buoyancy-driven circulation. The third point is the existence of two timescales linked to the first two points. Significant spatio-temporal changes in mixing can modify the tracer circulation on timescales that range from a few decades in the upper ocean to millennia in the abyss. Any tracer advected by the circulation will almost immediately 'feel' such changes in mixing (similar to row 2) and will additionally be impacted by mixing on a much longer timescale, associated with the slow changes in the underlying dynamics (row 3).

Discussion

We have used a range of observation-based estimates of diapycnal mixing to quantify the role of such mixing within the AMOC, i.e. the extent to which water and tracers are transferred diapycnally as they flow from the North Atlantic to the Southern Ocean. Our results indicate that diapycnal mixing contributes modestly but significantly to the AMOC's closure: up to 4 Sv of NADW upwell diabatically in the ocean interior. While this finding confirms that the AMOC's representation as a mainly adiabatic circulation (commonly assumed by theoretical and numerical modelling works) is reasonable, it also highlights the potential importance of diapycnal mixing for a range of problems – particularly those involving tracers.

Such importance can be illustrated in two ways. First, we have shown that the residual water mass transformation across any given isopycnal in the deep Atlantic, however small, may stem from potentially much larger individual diapycnal up- and downwelling contributions (Figure 3). This suggests that tracer exchanges between density layers may be significantly more vigorous than generally recognized. The covariance between the spatial pattern of mixing and the distribution of a tracer on any given isopycnal will determine the extent to which mixing redistributes the tracer vertically. This inference points to a key sampling issue: while data coverage may be adequate to map ϵ (see e.g. Waterhouse et al., 2014; Whalen et al., 2015; Kunze, 2017b), our work suggests that sparse sampling, especially in the vicinity of topography where upwelling is focussed, can make it very challenging to characterize the impact of mixing on the vertical transfer of tracers.

Second, setting this mixing-tracer covariance issue aside, an initial estimate of the impact of mixing on tracer transfer has been obtained by means of a bulk diffusive length scale, which characterises the vertical distance of mixing-induced tracer transport within the AMOC. This indicates that tracers within the southward-flowing NADW may undergo a substantial diapycnal transfer (equivalent to hundreds of metres in the vertical) to lighter or denser water masses, with potential entrainment into the AMOC's northward branch or, more likely, divergent global pathways and ventilation timescales after upwelling in the Southern Ocean. We highlighted this result with tracer injections in an idealized model of the AMOC. The impact of vertical variations in mixing on tracers was two-fold: first, mixing directly redistributes tracers between different water masses, altering their ventilation pathways and timescales. Second, mixing shapes the basin-scale overturning circulation on centennial-to-millennial timescales, thus indirectly influencing the tracers' global pathways. These two impacts are comparably important for tracer concentrations, but act on very different timescales.

While our key results are qualitatively endorsed by all four estimates of diapycnal mixing considered, the quantitative discrepancies between such estimates should be noted. Most glaringly, the bulk estimate from Lumpkin and Speer (2007) returns a maximum transformation rate of up to ∼4 Sv, substantially higher than the rates of ∼1-2 Sv produced by the localized (based on Argo floats, CTD and microstructure data) and a process-based (a theoretical description of internal tide breaking in the deep ocean) estimates. This second group of estimates all have significant uncertainties intrinsic to the parameterizations used to infer mixing (Polzin et al., 2014; Whalen et al., 2015; de Lavergne et al., 2020) that are challenging to quantify. Estimates of dissipation rate inferred from Argo floats and CTD

profiles depend on choices made in applying the strain-based parameterization, e.g. the length of the vertical segments and number of observations selected for averaging, and the shear-to-strain ratio (Kunze et al., 2006; Whalen et al., 2012, 2015; Kunze, 2017a, 2017b). Here, we averaged the individual estimates over a wide area (the entire Atlantic Ocean), thus mitigating the effect of uncertainties in each individual estimate (Whalen et al., 2015; Kunze, 2017a). The uncertainty associated with the internal tidal mixing estimate depends on the assumptions made about the horizontal and vertical propagation of the low- and high-mode internal tides. The bulk diffusivity estimate depends on the accuracy of the horizontal transports estimated in the inverse model, which themselves depend on uncertainties in the air-sea fluxes used and a partially subjective treatment of asynoptic observations. At any rate, although these uncertainties may be of potential significance and motivate further work, the similarity between the results from the different mixing estimates is encouraging, and suggests that broad patterns of mixing and water mass transformation diagnosed here are robust.

The uncertainties listed above may partially explain the large difference between the water mass transformation arising from the localized and tidal estimates and that from the inverse method. However, it is likely that such discrepancy also stems from the inability of Argo float and CTD data to capture turbulent processes in proximity to ocean boundaries, and the lack of representation of all boundary processes in the tidally-driven mixing estimate employed here. Among such near boundary turbulence hot spots are narrow passages between basins and deep trenches (M. Alford et al., 2013; Voet et al., 2015; Van Haren et al., 2017; Van Haren, 2018), continental slopes (J. D. Nash et al., 2004; J. Nash et al., 2007), mid-ocean ridges (St Laurent et al., 2001; Thurnherr & St. Laurent, 2011), seamounts (Lueck & Mudge, 1997; Toole et al., 1997; Kunze & Toole, 1997; Mashayek et al., 2021) and canyons (Carter & Gregg, 2002; Kunze et al., 2012).

Boundary processes, while not included explicitly in the bulk inverse estimate, are implicitly accounted for by this approach, which closes the buoyancy budget of the basin, within the constraints imposed by observed hydrographic sections. Our results add to evidence from recent studies in other deep-ocean regions that have also found a discrepancy between bulk estimates of mixing and those based on localized measurements (Huussen et al., 2012; Voet et al., 2015; Mashayek, Ferrari, et al., 2017). Evidence of enhanced mixing in the vicinity of western boundaries in the Atlantic Ocean has been previously reported (Stober et al., 2008; Kohler et al., 2014), but the implications for basin-integrated diapycnal upwelling of water masses and tracers have not yet been determined. A further caveat to our results is the omission of variations in the flux coefficient connecting the rates of turbulent energy dissipation and mixing; it is now established that such variations occur, and that they can alter the spatial pattern of mixing on basin scales (see de Lavergne, Madec, Le Sommer, et al. (2016); Mashayek, Salehipour, et al. (2017); M. Gregg et al. (2018); Cimoli et al. (2019) and references therein). Finally, the residence time of tracers, i.e. the time a tracer spends over regions with various mixing levels, is next to impossible to measure directly, yet has been suggested to be important in reconciling local and bulk estimates of mixing (Mashayek, Ferrari, et al., 2017).

To conclude, our results suggest that diapycnal mixing within the AMOC is likely to be a significant player in determining the global-scale pathways and residence times of tracers in the deep ocean. As such, we propose that a realistic representation of this mixing in the Atlantic Ocean may be necessary to understand and credibly project the ongoing climate change.

Acknowledgments

A significant amount of data was assimilated in the mixing estimates that we used in this work, the collection of which took place after years of instrument development and hundreds of at-sea days, and would not have been possible without the hard work and skill of the Captain and crew of each research vessel. We thank Rick Lumpkin for providing the estimate

of diffusivity in the Atlantic Ocean from his inverse solution. We thank Max Nikurashin for sharing the SAMBUCA code of Nikurashin and Vallis (2012). L.C. thanks support from the Clarendon Scholarship and the UK Natural Environment Research Council (NERC) via the DTP in Environmental Research (NE/L002612/1). A.M. acknowledges support from National Environmental Research Council (NE/P018319/1). H.L.J. and D.P.M. acknowledge support from the NERC UK-OSNAP and SNAP-DRAGON grants (NE/K010948/1, NE/T013494/1). C.B.W. was supported by the National Science Foundation OCE-1923558.

Data Availability

The CTD-based estimate of diapycnal mixing is available at the repository shared by Kunze (2017b), at `ftp.nwra.com/outgoing/kunze/iwturb`. The internal tide turbulence estimate, together with the corresponding hydrographic climatology, are available at the repository shared by de Lavergne et al. (2020), at `https://www.seanoe.org/data/00619/73082/`. The microstructure data is available at microstructure.ucsd.edu. The Argo-based turbulence estimate is available upon request from C.B.W., and the profile of diapycnal mixing from the inverse model of Lumpkin and Speer (2007) is available upon request from Rick Lumpkin.

References

Adcroft, A., Scott, J. R., & Marotzke, J. (2001). Impact of geothermal heating on the global ocean circulation. *Geophysical Research Letters*, *28*(9), 1735–1738.

Alford, M., Girton, J., Voet, G., Carter, G., Mickett, J., & Klymak, J. (2013). Turbulent mixing and hydraulic control of abyssal water in the samoan passage. *Geophysical Research Letters*, *40*(17), 4668-4674.

Alford, M. H. (2020). Global calculations of local and remote near-inertial-wave dissipation. *Journal of Physical Oceanography*, *50*(11), 3157–3164.

Bouffard, D., & Boegman, L. (2013). A diapycnal diffusivity model for stratified environmental flows. *Dynamics of Atmospheres and Oceans*, *61*, 14–34.

Bower, A. S., Lozier, M. S., Gary, S. F., & Böning, C. W. (2009). Interior pathways of the north atlantic meridional overturning circulation. *Nature*, *459*(7244), 243.

Buizert, C., Adrian, B., Ahn, J., Albert, M., Alley, R. B., Baggenstos, D., ... others (2015). Precise interpolar phasing of abrupt climate change during the last ice age. *Nature*, *520*(7549), 661–665.

Burke, A., Stewart, A. L., Adkins, J. F., Ferrari, R., Jansen, M. F., & Thompson, A. F. (2015). The glacial mid-depth radiocarbon bulge and its implications for the overturning circulation. *Paleoceanography*, *30*(7), 1021–1039.

Carter, G. S., & Gregg, M. C. (2002). Intense, variable mixing near the head of monterey submarine canyon. *Journal of Physical Oceanography*, *32*(11), 3145–3165.

Caulfield, C. (2020). Layering, instabilities, and mixing in turbulent stratified flows. *Annual Review of Fluid Mechanics*, *53*.

Cessi, P. (2019). The global overturning circulation. *Annual review of marine science*, *11*, 249–270.

Cimoli, L., Caulfield, C.-c. P., Johnson, H. L., Marshall, D. P., Mashayek, A., Naveira Garabato, A. C., & Vic, C. (2019). Sensitivity of deep ocean mixing to local internal tide breaking and mixing efficiency. *Geophysical Research Letters*, *43*, 14,622–14,633.

Cunningham, S. A., Kanzow, T., Rayner, D., Baringer, M. O., Johns, W. E., Marotzke, J., ... others (2007). Temporal variability of the atlantic meridional overturning circulation at 26.5 n. *science*, *317*(5840), 935–938.

Davies, J., & Davies, D. (2010). Earth's surface heat flux. *Solid Earth*, *1*, 5-24.

de Lavergne, C., Groeskamp, S., Zika, J., & Johnson, H. L. (2022). The role of mixing in the large-scale ocean circulation. *Ocean mixing*, 35–63.

de Lavergne, C., Madec, G., Le Sommer, J., Nurser, A., & Naveira-Garabato, A. (2016). The impact of a variable mixing efficiency on the abyssal overturning. *Journal of*

Physical Oceanography, *46*, 663-681.

de Lavergne, C., Madec, G., Roquet, F., Holmes, R., & McDougall, T. (2017). Abyssal ocean overturning shaped by seafloor distribution. *Nature*, *551*, 181-186.

de Lavergne, C., Madec, G., Sommer, J. L., Nurser, G., & Garabato, A. N. (2016). On the consumption of antarctic bottom water in the abyssal ocean. *Journal of Physical Oceanography*, *46*(2), 635–661.

de Lavergne, C., Vic, C., Madec, G., Roquet, F., Waterhouse, A. F., Whalen, C., ... Hibiya, T. (2020). A parameterization of local and remote tidal mixing. *Journal of Advances in Modeling Earth Systems*, *12*(5).

Drake, H. F., Ferrari, R., & Callies, J. (2020). Abyssal circulation driven by near-boundary mixing: Water mass transformations and interior stratification. *Journal of Physical Oceanography*, *50*(8), 2203–2226.

Ferrari, R., Mashayek, A., McDougall, T., Nikurashin, M., & Champin, J.-M. (2016). Turning ocean mixing upside down. *Journal of Physical Oceanography*, *46*, 2239-2261.

Fine, R. A., Rhein, M., & Andrié, C. (2002). Using a cfc effective age to estimate propagation and storage of climate anomalies in the deep western north atlantic ocean. *Geophysical Research Letters*, *29*(24), 80–1.

Forget, G., Champin, J.-M., Heimbach, P., Hill, C., Ponte, R., & Wunsch, C. (2015). Ecco version 4: An integrated framework for non-linear inverse modeling and global ocean state estimation. *Geosci. Model Dev.*, *8*, 3071-3104.

Forget, G., & Ferreira, D. (2019). Global ocean heat transport dominated by heat export from the tropical pacific. *Nature Geoscience*, *12*(5), 351–354.

Ganachaud, A. (2003). Large-scale mass transport, water mass formation and diffusivities estimated from world ocean circulation experiment (woce) hydrographic data. *J. Geophys. Res.*, *108*, 3213.

Gnanadesikan, A. (1999). A simple predictive model for the structure of the oceanic pycnocline. *Science*, *208*, 2077-2079.

Gouretski, V., & Koltermann, K. P. (2004). Woce global hydrographic climatology. *Berichte des BSH*, *35*, 1–52.

Gregg, M., D'Asaro, E., Riley, J., & Kunze, E. (2018). Mixing efficiency in the ocean. *Annual review of marine science*, *10*, 443–473.

Gregg, M., & Kunze, E. (1991). Shear and strain in santa monica basin. *J. Geophys. Research*, *96*, 16709-16719.

Gregg, M. C., Sanford, T. B., & Winkel, D. P. (2003). Reduced mixing from the breaking of internal waves in equatorial waters. *Nature*, *422*(6931), 513–515.

Groeskamp, S., Griffies, S. M., Iudicone, D., Marsh, R., Nurser, A. G., & Zika, J. D. (2019). The water mass transformation framework for ocean physics and biogeochemistry. *Annual review of marine science*, *11*, 271–305.

Gruber, N., Clement, D., Carter, B. R., Feely, R. A., Van Heuven, S., Hoppema, M., ... others (2019). The oceanic sink for anthropogenic co2 from 1994 to 2007. *Science*, *363*(6432), 1193–1199.

Holmes, R. M., de Lavergne, C., & Mcdougall, T. J. (2019). Tracer transport within abyssal mixing layers. *Journal of Physical Oceanography*, *49*(10), 2669–2695.

Holzer, M., Primeau, F. W., Smethie Jr, W. M., & Khatiwala, S. (2010). Where and how long ago was water in the western north atlantic ventilated? maximum entropy inversions of bottle data from woce line a20. *Journal of Geophysical Research: Oceans*, *115*(C7).

Huussen, T., Naveira-Garabato, A., Bryden, H., & McDonagh, E. (2012). Is the deep indian ocean moc sustained by breaking internal waves? *Journal of Geophysical Research: Oceans*, *117*.

Jackett, D., & McDougall, T. (1997). A neutral density variable for the world's oceans. *Journal of Physical Oceanography*, *27*, 237-263.

Johnson, H. L., Cessi, P., Marshall, D. P., Schloesser, F., & Spall, M. A. (2019). Recent contributions of theory to our understanding of the atlantic meridional overturning

circulation. *Journal of Geophysical Research: Oceans*, *124*(8), 5376–5399.

Klocker, A., & McDougall, T. J. (2010). Influence of the nonlinear equation of state on global estimates of dianeutral advection and diffusion. *Journal of Physical Oceanography*, *40*(8), 1690–1709.

Kohler, J., Mertens, C., Walter, M., Stober, U., Rhein, M., & Kanzow, T. (2014). Variability in the internal wave field induced by the atlantic deep western boundary current at 16°n. *J. Phy. Oceanogr.*, *44*.

Kunze, E. (2017a). The internal-wave-driven meridional overturning circulation. *Journal of Physical Oceanography*, *47*, 2673-2689.

Kunze, E. (2017b). Internal-wave-driven mixing: Global geography and budgets. *Journal of Physical Oceanography*, *47*, 1325–1345.

Kunze, E., Firing, E., Hummon, J., Chereskin, T., & Thurnherr, A. (2006). Global abyssal mixing inferred from lowered adcp shear and ctd strain profiles. *J. Phy. Oceanogr.*, *36*, 1553-1576.

Kunze, E., MacKay, C., McPhee-Shaw, E. E., Morrice, K., Girton, J. B., & Terker, S. R. (2012). Turbulent mixing and exchange with interior waters on sloping boundaries. *Journal of Physical Oceanography*, *42*(6), 910–927.

Kunze, E., & Toole, J. M. (1997). Tidally driven vorticity, diurnal shear, and turbulence atop fieberling seamount. *Journal of Physical Oceanography*, *27*(12), 2663–2693.

Lauvset, S. K., Key, R. M., Olsen, A., van Heuven, S., Velo, A., Lin, X., ... others (2016). A new global interior ocean mapped climatology: The 1× 1 glodap version 2. *Earth System Science Data*, *8*, 325–340.

Lueck, R. G., & Mudge, T. D. (1997). Topographically induced mixing around a shallow seamount. *Science*, *276*(5320), 1831–1833.

Lumpkin, R., & Speer, K. (2007). Global ocean meridional overturning. *Journal of Physical Oceanography*, *37*, 2550-2562.

MacGilchrist, G. A., Marshall, D. P., Johnson, H. L., Lique, C., & Thomas, M. (2017). Characterizing the chaotic nature of ocean ventilation. *Journal of Geophysical Research: Oceans*, *122*(9), 7577–7594.

Marshall, J., & Speer, K. (2012). Closure of the meridional overturning circulation through southern ocean upwelling. *Nature geoscience*, *5*, 171-180.

Mashayek, A., Caulfield, C., & Peltier, W. (2013). Time dependent, non-monotonic mixing in stratified turbulent shear flows: implications for oceanographic estimates of buoyancy flux. *Journal of Fluid Mechanics*, *736*, 570-593.

Mashayek, A., Ferrari, R., M., & Peltier, W. (2015). Influence of enhanced abyssal diapycnal mixing on stratification and the ocean overturning circulation. *Journal of Physical Oceanography*, *45*, 2580–2597.

Mashayek, A., Ferrari, R., Merrifield, S., Ledwell, J., St Laurent, L., & Naveira-Garabato, A. (2017). Topographic enhancement of vertical turbulent mixing in the southern ocean. *Nature Communications*, *8*.

Mashayek, A., Gula, J., Baker, L., Garabato, A. N., Cimoli, L., & Riley, J. (2021). Mountains to climb: on the role of seamounts in upwelling of deep ocean waters.

Mashayek, A., & Peltier, W. (2013). Shear induced mixing in geophysical flows: Does the route to turbulence matter to its efficiency? *Journal of Fluid Mechanics*, *725*, 216-261.

Mashayek, A., Salehipour, H., Bouffard, D., Caulfield, C., Ferrari, R., Nikurashin, M., ... Smyth, W. (2017). Efficiency of turbulent mixing in the abyssal ocean circulation. *Geophysical Research Letters*, *44*, 6296-6306.

McCarthy, G., Smeed, D., Johns, W. E., Frajka-Williams, E., Moat, B., Rayner, D., ... Bryden, H. (2015). Measuring the atlantic meridional overturning circulation at 26 n. *Progress in Oceanography*, *130*, 91–111.

McDougall, T., & Ferrari, R. (2017). Abyssal upwelling and downwelling driven by near-boundary mixing. *J. Phys. Oceanogr.*, *47*, 261–283. doi: 10.1175/JPO-D-16-0082.1

Nash, J., Alford, M., Kunze, E., Martini, K., & Kelly, S. (2007). Hotspots of deep ocean mixing on the oregon continental slope. *Geophysical Research Letters*, *34*(1).

Nash, J. D., Kunze, E., Toole, J. M., & Schmitt, R. W. (2004). Internal tide reflection and turbulent mixing on the continental slope. *Journal of Physical Oceanography*, *34*(5), 1117–1134.

Naveira-Garabato, A., Williams, A., & Bacon, S. (2014). The three-dimensional overturning circulation of the southern ocean during the woce era. *Progress in Oceanography*, *120*, 41-78.

Nikurashin, M., & Ferrari, R. (2011). Global energy conversion rate from geostrophic flows into internal lee waves in the deep ocean. *Geophysical Research Letters*, *38*(8).

Nikurashin, M., & Vallis, G. (2012). A theory of the interhemispheric meridional overturning circulation and associated stratification. *Journal of Physical Oceanography*, *42*(10), 1652–1667.

Osborn, T. (1980). Estimates of the local-rate of vertical diffusion from dissipation measurements. *Journal of Physical Oceanography*, *10*, 83-89.

Polzin, K., Naveira-Garabato, A., Huussen, T., Sloyan, B., & Waterman, S. (2014). Finescale parameterizations of turbulent dissipation. *J. Geophys. Research*, *119*, 1383-1419.

Reid, J. L. (1994). On the total geostrophic circulation of the north atlantic ocean: Flow patterns, tracers, and transports. *Progress in Oceanography*, *33*(1), 1–92.

Rhein, M., Kieke, D., & Steinfeldt, R. (2015). Advection of n orth a tlantic d eep w ater from the l abrador s ea to the southern hemisphere. *Journal of Geophysical Research: Oceans*, *120*(4), 2471–2487.

Santoso, A., England, M., & Hirst, A. (2006). Circumpolar deep water circulation and variability in a coupled climate model. *J. Phys. Oceanogr.*, *36*, 1523-1552.

Sloyan, B., & Rintoul, S. (2001). The southern ocean limb of the global deep overturning circulation. *J. Phys. Oceanogr.*, *31*, 143-173.

Smeed, D., McCarthy, G., Cunningham, S., Frajka-Williams, E., Rayner, D., Johns, W. E., ... others (2014). Observed decline of the atlantic meridional overturning circulation 2004-2012. *Ocean Science*, *10*(1), 29–38.

Spingys, C. P., Naveira Garabato, A. C., Legg, S., Polzin, K. L., Abrahamsen, E. P., Buckingham, C. E., ... Frajka-Williams, E. E. (2021). Mixing and transformation in a deep western boundary current: A case study. *Journal of Physical Oceanography*, *51*(4), 1205–1222.

Srokosz, M., & Bryden, H. (2015). Observing the atlantic meridional overturning circulation yields a decade of inevitable surprises. *Science*, *348*(6241), 1255575.

St Laurent, L., Toole, J. M., & Schmitt, R. W. (2001). Buoyancy forcing by turbulence above rough topography in the abyssal brazil basin. *Journal of Physical Oceanography*, *31*(12), 3476–3495.

Stober, U., Walter, M., Mertens, C., & Rhein, M. (2008). Mixing estimates from hydrographic measurements in the deep western boundary current of the north atlantic. *Deep Sea Research Part I: Oceanographic Research Papers*, *55*, 721-736.

Talley, L. D. (1996). North atlantic circulation and variability, reviewed for the cnls conference. *Physica D: Nonlinear Phenomena*, *98*(2-4), 625–646.

Talley, L. D. (2013). Closure of the Global Overturning Circulation trough the Indian, Pacific, and Southern Oceans. *Oceanography*, *26*, 80-97.

Talley, L. D., Reid, J. L., & Robbins, P. E. (2003). Data-based meridional overturning streamfunctions for the global ocean. *Journal of Climate*, *16*(19), 3213–3226.

Thurnherr, A. M., & St. Laurent, L. C. (2011). Turbulence and diapycnal mixing over the east pacific rise crest near 10 n. *Geophysical research letters*, *38*(15).

Toggweiler, J., & Samuels, B. (1998). On the ocean's large-scale circulation near the limit of no vertical mixing. *J. Phys. Oceanogr.*, *28*, 1832–1852.

Toole, J. M., Schmitt, R. W., Polzin, K. L., & Kunze, E. (1997). Near-boundary mixing above the flanks of a midlatitude seamount. *Journal of Geophysical Research: Oceans*, *102*(C1), 947–959.

Van Haren, H. (2018). *High-resolution observations of internal wave turbulence in the deep ocean*. Springer Oceanography. Springer, Cham. (In: Velarde M., Tarakanov R., Marchenko A. (eds) The Ocean in Motion.)

Van Haren, H., Berndt, C., & Klaucke, I. (2017). Ocean mixing in deep-sea trenches: New insights from the challenger deep, mariana trench. *Deep-Sea Research*, *129*, 1-9.

Voet, G., Girton, G., Alford, M., Carter, G., Klymak, J., & Mickett, J. (2015). Pathways, volume transport, and mixing of abyssal water in the samoan passage. *J. Phys. Oceanogr.*, *45*, 562–588.

Waterhouse, A., MacKinnon, J., Nash, J., Alford, M., Kunze, E., Simmons, H., ... Lee, C. (2014). Global patterns of diapycnal mixing from measurements of the turbulent dissipation rate. *Journal of Physical Oceanography*, *44*, 1854–1872.

Waterman, S., Polzin, K. L., Naveira Garabato, A. C., Sheen, K. L., & Forryan, A. (2014). Suppression of internal wave breaking in the antarctic circumpolar current near topography. *Journal of Physical Oceanography*, *44*(5), 1466–1492.

Whalen, C., MacKinnon, J., Talley, L., & Waterhouse, A. (2015). Estimating the mean diapycnal mixing using a finescale strain parameterization. *J. Phys. Oceanogr.*, *45*, 1174-1188.

Whalen, C., Talley, L., & MacKinnon, J. (2012). Spatial and temporal variability of global ocean mixing inferred from argo profiles. *Geophys. Res. Lett.*, *39*. (L18612, doi:10.1029/2012GL053196)

Wijesekera, H., Padman, L., Dillon, T., Levine, M., Paulson, C., & Pinkel, R. (1993). The application of internal-wave dissipation models to a region of strong mixing. *Journal of physical oceanography*, *23*(2), 269–286.

Wolfe, C., & Cessi, P. (2011). The adiabatic pole-to-pole overturning circulation. *J. Phys. Oceanogr.*, *41*, 1795-1810.

Zhai, X., Greatbatch, R. J., Eden, C., & Hibiya, T. (2009). On the loss of wind-induced near-inertial energy to turbulent mixing in the upper ocean. *Journal of Physical Oceanography*, *39*(11), 3040–3045.

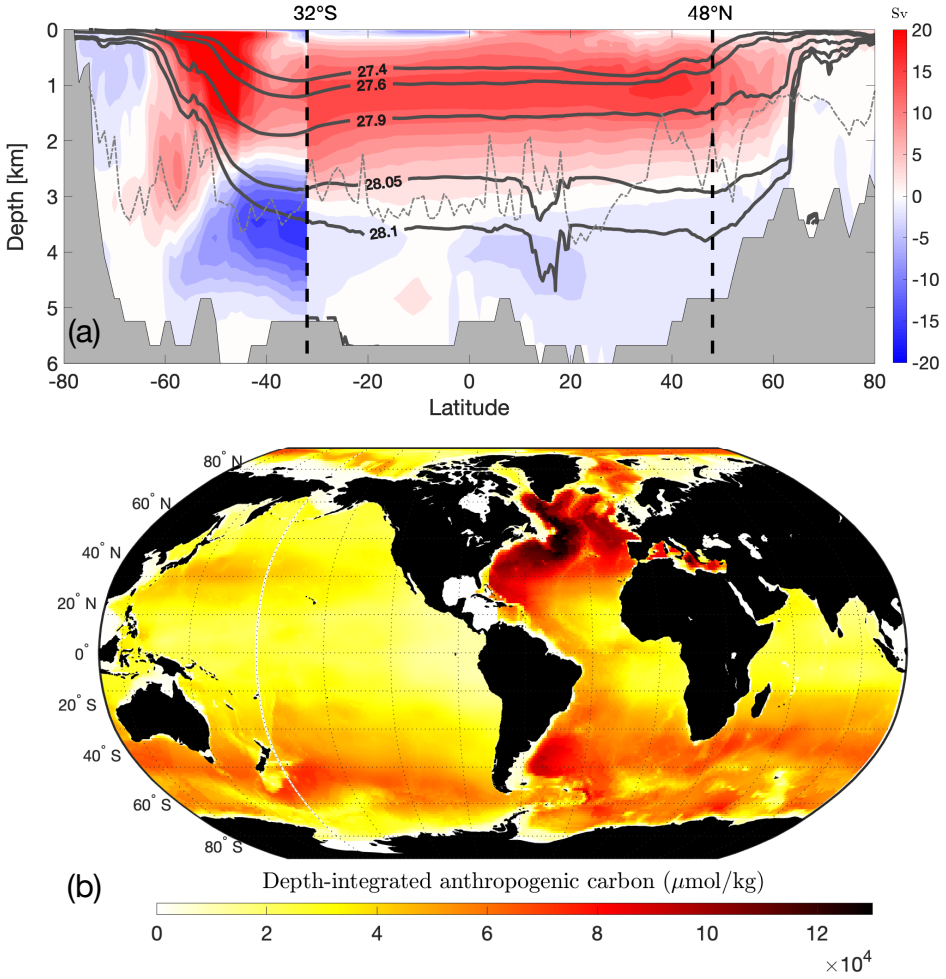

Figure 1. (a) Overturning streamfunction from ECCO ocean state estimate (Forget et al., 2015), calculated for the Atlantic Ocean only between 80°N and 32°S, and globally in the Southern Ocean between 32°S and 80°S (hence the discontinuity at 32°S). The maximum transport of the AMOC is 17 Sv. Contours are every 2 Sv. The thick black lines denote the zonally averaged neutral density levels, calculated from the World Ocean Circulation Experiment (WOCE; (Gouretski & Koltermann, 2004)) climatology. The dashed gray line indicates the average depth of the crest of the Mid-Atlantic Ridge. (b) Depth-integrated concentration of anthropogenic carbon from GLODAP climatology (Lauvset et al., 2016).

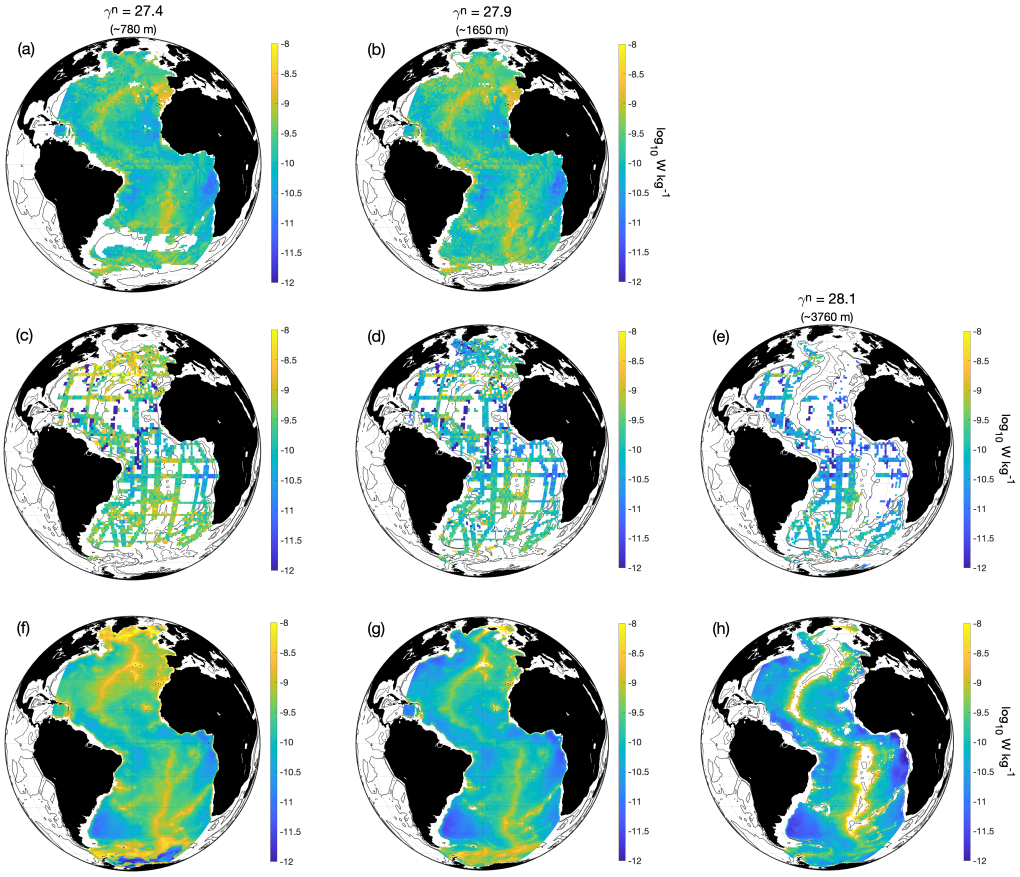

Figure 2. Rate of dissipation of turbulent kinetic energy ϵ estimated from (a-b) Argo float data (extending work of Whalen et al. (2015)), (c-e) CTD and microstructure data (based on Kunze (2017b) and (Waterhouse et al., 2014)), and (f-h) internal tides (from de Lavergne et al. (2020)), shown on the density surfaces $\gamma^n = 27.4$ (left column), $\gamma^n = 27.9$ (middle column), and $\gamma^n = 28.1$ (right column). The average depth of the density surfaces in the Atlantic Ocean is also shown.

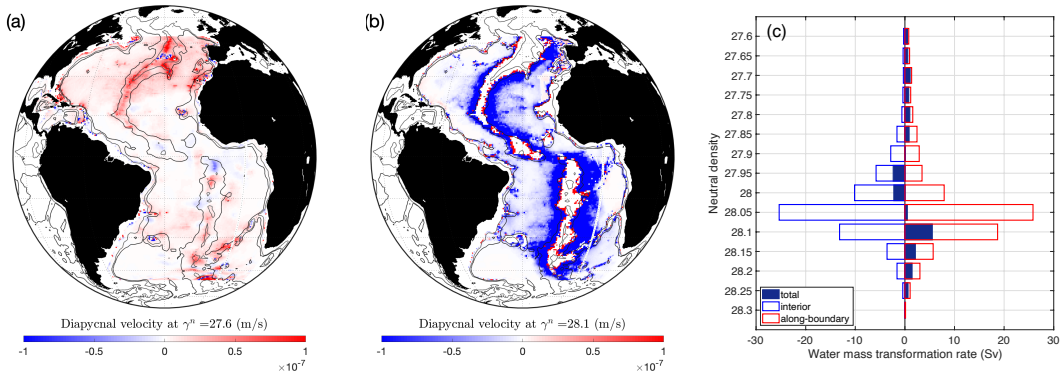

Figure 3. (a-b) Diapycnal velocity (Equation 2) calculated from the tidally-driven mixing estimate on the density surfaces $\gamma^n = 27.6$ (a) and $\gamma^n = 28.1$ (b). Positive values (red) indicate diapycnal upwelling, and negative values (blue) indicate diapycnal downwelling. The 3000 m and 4000 m isobaths are also shown (thin black lines). (c) Water mass transformation rate (Equation 3) for the tidally-driven mixing estimate across the density surfaces of the NADW flow ($\gamma^n = 27.6 - 28.15$) and the abyssal waters below ($\gamma^n > 28.15$). The contributions of along-boundary and interior water mass transformations are shown by the empty red and blue bars, respectively, while their residual is shown by the filled blue bar. Positive transformation corresponds to a decrease of density.

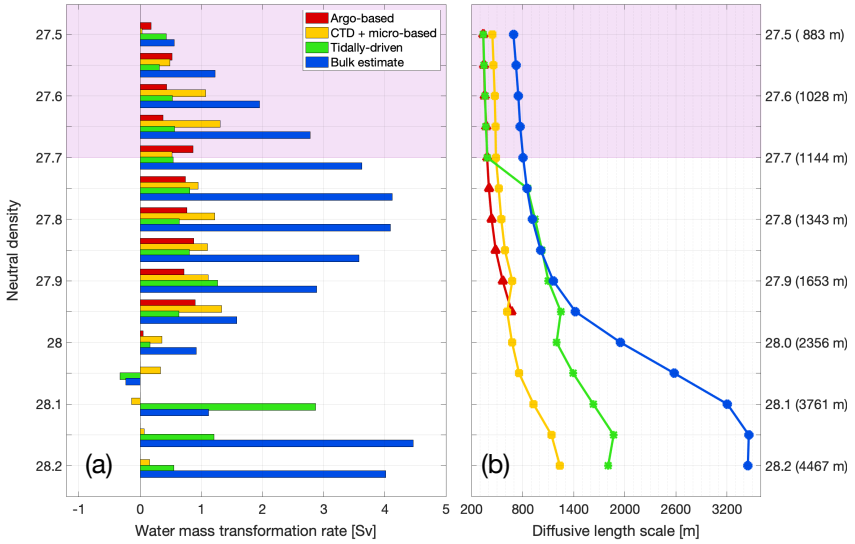

Figure 4. (a) Water mass transformation rate and (b) diffusive length scale calculated from the Argo-based estimate of diapycnal mixing (red), CTD data+microstructure profile-based estimate (yellow), tidally-driven diapycnal mixing estimate (green), and the bulk estimate of diapycnal mixing from Lumpkin and Speer (2007) (blue). The y-axis in panel (b) reports the mean depth of each density surface in the Atlantic Ocean between 48°N and 32°S. Pink shading indicates the density range separating the southward and northward flows of the AMOC (i.e. the layer of near-zero transport). Note that areas with no data in Figure 2 don't contribute to the transformation rates in panel (a).

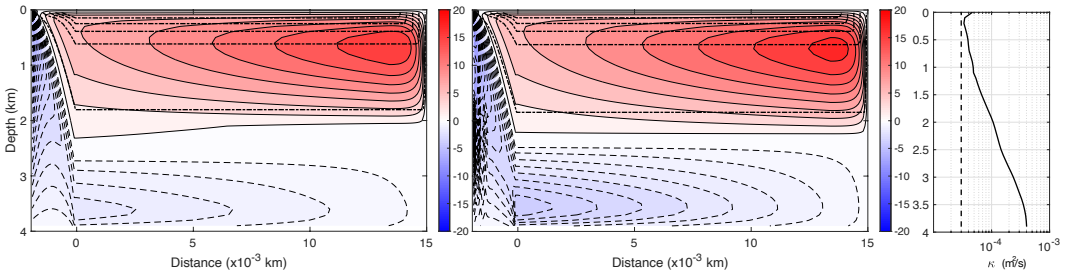

Figure 5. Overturning streamfunction in a zonally-averaged model of the Atlantic Ocean. The model parameters closely follow those of Nikurashin and Vallis (2012), except for the vertical diffusivity profile. Two cases are considered: left panel uses a constant vertical diffusivity of 3×10^{-5} m^2/s, chosen from the CTD-based estimate of (Kunze, 2017b), and the middle panel shows a vertically-variable diffusivity based on the bulk estimate of Lumpkin and Speer (2007) (for the Atlantic Ocean), hereafter referred to as κ_{LS07}. The two diffusivities are compared in the right panel.

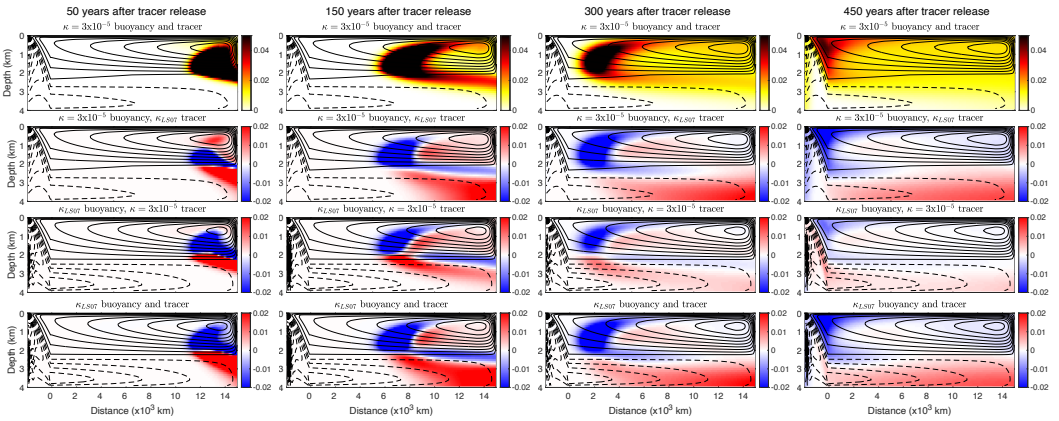

Figure 6. Time evolution of a passive tracer in a zonally-averaged model of the Atlantic Ocean circulation. The tracer is injected at the surface in the northern hemisphere with values increasing linearly from 0 at the equator to 1 at the northernmost point. Time evolves from left to right, from year 50 after tracer release in the left column to 150, 300, and 450 years in the other columns. Top row shows the tracer concentration when both tracer and buoyancy are subject to the same constant diffusivity of 3×10^{-5} m^2/s. Rows 2-4 show perturbation simulations in which either buoyancy, or tracer, or both, are subjected to a vertically variable diffusivity based on the Lumpkin and Speer (2007) bulk estimate, with the colors indicating the difference between the tracer concentration for each row and that in the 'control' simulation of the top row. In all panels, contours of the meridional overturning streamfunction are shown by solid lines for the AMOC upper cell, and dashed lines for the abyssal cell. The overturnings for rows 1 and 2 are the same as the left panel in Figure 5, and those for rows 3 and 4 are the same as the middle panel in Figure 5.